

# PHOTONICS Research

## Spatiospectral transformation of noncollimated light beams diffracted by ultrasound in birefringent crystals

ALEXEY V. GOREVOY,  ALEXANDER S. MACHIKHIN,\*  GRIGORIY N. MARTYNOV, AND VITOLD E. POZHAR 

Laboratory of Acousto-optic Spectroscopy, Scientific and Technological Center of Unique Instrumentation, Russian Academy of Sciences, Moscow 117342, Russia

\*Corresponding author: machikhin@ntcup.ru

Received 17 December 2020; revised 16 February 2021; accepted 17 February 2021; posted 19 February 2021 (Doc. ID 417992); published 21 April 2021

Spatiospectral structure of wave phase matching in birefringent crystals has a strong dependence on the geometry of the acousto-optic interaction and incident light spectrum. This dependence defines details of light beam profile transformation. It is especially important for imaging applications related to a large angular aperture and a wide spectral bandwidth of the incident light. In this paper, we demonstrate accurate three-dimensional plotting of a light transmission pattern without small birefringence approximation. The rather complicated shape of the phase-matching locus in the spatio-spectral domain inevitably leads to residual spatially nonuniform chromatic aberrations in the spectral image. Theoretical consideration and computational modeling are confirmed by the experiments on Bragg diffraction in paratellurite crystal. The results are especially important for the development of acousto-optical imaging devices and laser beam shaping technologies. © 2021 Chinese Laser Press

<https://doi.org/10.1364/PRJ.417992>

### 1. INTRODUCTION

Acousto-optic (AO) interaction is mainly associated with light diffraction by ultrasound waves in solid, liquid, and gas media [1–3]. Depending on the properties of the medium and the relationship between light and sound parameters, this phenomenon may be used for spectral and spatial filtration, deflection, intensity modulation, and other transformations of the incident beam [4,5]. Devices based on this principle have multiple applications in optical engineering and photonics. The main equations describing AO interaction (phase-matching conditions) may be derived from the laws of conservation of energy and momentum for photons and a phonon:

$$\omega_d = \omega_i \pm f, \quad (1a)$$

$$\mathbf{k}_d = \mathbf{k}_i \pm \mathbf{q}, \quad (1b)$$

where  $(f, \mathbf{q})$ ,  $(\omega_i, \mathbf{k}_i)$ , and  $(\omega_d, \mathbf{k}_d)$  are the frequencies and wavevectors of sound, incident light, and diffracted light. The sign “+” corresponds to the absorption of the phonon, and the sign “−” corresponds to its stimulated birth. Due to great difference between the frequencies of interacting acoustic  $f$  and optical  $\omega_i$  waves, the main geometrical and spectral relations describing AO interaction may be derived from Eq. (1b). In practice, because of the finite angular aperture and spectral bandwidth of the incident light, acoustic energy

walk-off and other factors, light field distribution  $U_d(\mathbf{k}_d)$  after diffraction on acoustic field  $A(\mathbf{q})$  may be represented as a sum of plane-wave interactions [6]:

$$\begin{aligned} U_d(\mathbf{k}_d) &= \int \int_{-\infty}^{+\infty} U_i(\mathbf{k}_i) A(\mathbf{q}) \delta(\mathbf{k}_d - \mathbf{k}_i - \mathbf{q}) d\mathbf{k}_i d\mathbf{q} \\ &= \int_{-\infty}^{+\infty} U_i(\mathbf{k}_i) A(\mathbf{k}_d - \mathbf{k}_i) d\mathbf{k}_i, \end{aligned} \quad (2)$$

where  $\delta$  is the Dirac delta function. Wavevectors are defined by direction vectors and wavelengths or frequencies:

$$\mathbf{q}(f, \mathbf{e}_q) = (2\pi/\Lambda) \mathbf{e}_q = [2\pi f/V(\mathbf{e}_q)] \mathbf{e}_q, \quad (3a)$$

$$\mathbf{k}_i(\lambda_{i0}, \mathbf{e}_{ki}) = (2\pi/\lambda_i) \mathbf{e}_{ki} = [2\pi n_i(\lambda_{i0}, \mathbf{e}_{ki})/\lambda_{i0}] \mathbf{e}_{ki}, \quad (3b)$$

$$\mathbf{k}_d(\lambda_{d0}, \mathbf{e}_{kd}) = (2\pi/\lambda_d) \mathbf{e}_{kd} = [2\pi n_d(\lambda_{d0}, \mathbf{e}_{kd})/\lambda_{d0}] \mathbf{e}_{kd}, \quad (3c)$$

where  $\mathbf{e}_q$ ,  $\mathbf{e}_{ki}$ , and  $\mathbf{e}_{kd}$  are the unit vectors indicating the directions of wavevectors for sound, incident light, and diffracted light;  $\Lambda$ ,  $\lambda_i$ , and  $\lambda_d$  are the corresponding wavelengths in the AO medium;  $\lambda_{i0} \approx \lambda_{d0} = \lambda_0$  are the light wavelengths in a vacuum;  $V$  is the sound velocity; and  $n_i$  and  $n_d$  are the refractive indices.

The second equality in Eq. (2) is the convolution integral, where the acoustic field distribution  $A$  may be considered as the impulse response for monochromatic plane light wave of

amplitude  $U_i$ :  $U_i(\mathbf{k}_i) = U_i\delta(\mathbf{k}_i)$ . According to Eq. (3), length and direction of vector  $(\mathbf{k}_d - \mathbf{k}_i)$  have a strong dependence on the refractive indices  $n_i$  and  $n_d$  and may be represented as a function of  $\lambda_0$ ,  $\mathbf{e}_{ki}$ , and  $\mathbf{e}_{kd}$ . Thus, the main features of diffracted light field distribution are defined both by the structure of the acoustic field and the refractive properties of the medium. Therefore, light beam profile transformation as well as the key parameters of the AO device is defined by the spatio-spectral phase matching Eq. (2). This is especially crucial for spectral imaging and other AO applications related to wide angular aperture and wide spectral bandwidth of the incident light [7–9].

In this study, we show that spectral and angular characteristics of AO interaction are inseparable. This means the inevitable presence of residual spatially nonuniform chromatic aberrations in the diffracted beam after AO spectral filtration. For this purpose, we have theoretically and experimentally studied the transmission function  $T$  for AO Bragg diffraction in birefringent crystal  $\text{TeO}_2$ —the most effective and widely used AO material [10]. First, we derive the key formulas representing the angular and spectral dependencies of the phase mismatch. Second, we analyze the geometry of the phase-matching locus and demonstrate its topological diversity. Third, we support the theoretical analysis with experimental investigation.

## 2. THEORETICAL CONSIDERATIONS

Due to various configurations of anisotropic AO interaction, birefringent crystalline media have proven to be the most effective for multiple applications [5,11]. Figure 1 shows a typical wavevector diagram of anisotropic AO interaction in a uniaxial birefringent crystal like  $\text{TeO}_2$ . Each plane wave  $\mathbf{k}_i$  diffracts by an acoustic wave  $\mathbf{q}$  and changes the direction of the wavevector ( $\mathbf{e}_{ki} \rightarrow \mathbf{e}_{kd}$ ) and polarization ( $e \rightarrow o$  or  $o \rightarrow e$ ). We assume that the plane waves  $\mathbf{k}_{is}$ ,  $\mathbf{q}_s$ , and  $\mathbf{k}_{ds}$  are perfectly phase-matched according to Eq. (1b). The corresponding unit vectors specified by the pair of angles (azimuthal and polar) are described as follows:  $\mathbf{e}_{kis}(\varphi_i, \theta_i)$ ,  $\mathbf{e}_{qs}(\varphi_q, \gamma)$ , and  $\mathbf{e}_{kds}(\varphi_d, \theta_d)$ . The lengths of vectors  $\mathbf{k}_{is}$  and  $\mathbf{k}_{ds}$  depend on the refractive indices  $n_o(\lambda_0)$  and  $n_e(\lambda_0)$ ; the wavenumber  $k_0$  corresponds to light wavelength in a vacuum:  $k_0 = 2\pi/\lambda_0$ .

For description of optical beam transformation, we introduce coordinate systems for input ( $x'_i y'_i z'_i$ ) and diffracted beams ( $x'_d y'_d z'_d$ ) in the following way. For convenience, we consider the normal incidence on the input facet, so  $\mathbf{e}_{kis} = \mathbf{e}_{ki}$ . The axes  $z'_i$  and  $z'_d$  are directed

parallel to the optical beam trajectory. To find the angular transmission function, one needs to trace the pathway of each partial angular component  $\mathbf{e}'_{ki}$  of the input beam.

As the AO cell geometry is specified by the directions of incident light  $\mathbf{e}_{kis}$  and sound  $\mathbf{e}_{qs}$ , then the acoustic frequency  $f_s$  satisfying Eq. (1b) and Eq. (3) for a wavelength  $\lambda_s$  may be calculated (for  $e \rightarrow o$  interaction) as [12]

$$f_s = V(\mathbf{e}_{qs})n_o(\lambda_s)[\xi_s A_s - \sqrt{\xi_s^2(A_s^2 - 1) + 1}]/\lambda_s, \quad (4)$$

$$\xi(\lambda_0, \mathbf{e}_{ki}) = n_e(\lambda_0)/\sqrt{n_o^2(\lambda_0)\cos^2\theta_i + n_e^2(\lambda_0)\sin^2\theta_i}, \quad (5)$$

where geometrical parameter  $A_s = -\mathbf{e}_{kis} \cdot \mathbf{e}_{qs}$  and  $\xi$  is a birefringence parameter:  $\xi_s = \xi(\lambda_s, \mathbf{e}_{kis})$ . Thus, we find  $\mathbf{q}_s(f_s, \mathbf{e}_{qs})$  and  $\mathbf{k}_{ds} = \mathbf{k}_{is} + \mathbf{q}_s$  as a function of  $\lambda_s$ ,  $\mathbf{e}_{kis}$ , and  $\mathbf{e}_{qs}$ .

To describe AO diffraction of a divergent or convergent light beam, we decompose an input angular 2D distribution  $U_i(\mathbf{k}_i) = U_i(\lambda_0, \mathbf{e}_{ki})$  into a plane-wave spectrum and calculate diffracted light field distribution  $U_d(\mathbf{k}_d) = U_d(\lambda_0, \mathbf{e}_{kd})$  according to Eqs. (2) and (3). The commonly used analytical method describes the light beam transformation caused by diffraction on plane sound wave  $\mathbf{q}$  by introducing a wavevector mismatch  $\Delta\mathbf{k}$  into Eq. (1b) [11]:

$$\mathbf{k}_d = \mathbf{k}_i \pm \mathbf{q}_s + \Delta\mathbf{k}. \quad (6)$$

In this way, we replace  $A(\mathbf{k}_d - \mathbf{k}_i)$  in Eq. (2) by  $A(\mathbf{q}_s + \Delta\mathbf{k})$ . For a given  $\mathbf{q}_s$ , we can calculate  $\Delta\mathbf{k}(\lambda_0, \mathbf{e}_{ki}, \mathbf{e}_{kd})$  from Eq. (6) and use it as an argument of function  $A$  describing the acoustic field. With this approach, the diffracted light field may be represented as a composition of angular components characterized by the direction of wavevector  $\mathbf{e}_{kdm}$  and transmission function  $T(\lambda_0, \mathbf{e}_{ki})$  as follows [11,12]:

$$\mathbf{e}_{kdm}(\lambda_0, \mathbf{e}_{ki}) = \arg \min_{\mathbf{e}_{kd}} |\Delta\mathbf{k}(\lambda_0, \mathbf{e}_{ki}, \mathbf{e}_{kd})|, \quad (7)$$

$$\Delta\mathbf{k}_m(\lambda_0, \mathbf{e}_{ki}) = \Delta\mathbf{k}(\lambda_0, \mathbf{e}_{ki}, \mathbf{e}_{kdm}), \quad (8)$$

$$T(\lambda_0, \mathbf{e}_{ki}) = (\Gamma L)^2 \text{sinc}^2 \left[ L \sqrt{\Gamma^2 + (|\Delta\mathbf{k}_m|/2)^2} \right], \quad (9)$$

where  $\text{sinc}(x) = (\sin x)/x$ ,  $\Gamma$  is a coupling coefficient proportional to the effective photoelastic constant and acoustic wave amplitude, and  $L$  is a length of AO interaction. For  $e \rightarrow o$  interaction, the equations for  $\mathbf{k}_{dm}(\lambda_0, \mathbf{e}_{kdm})$  and  $|\Delta\mathbf{k}_m|$  may be derived analytically:

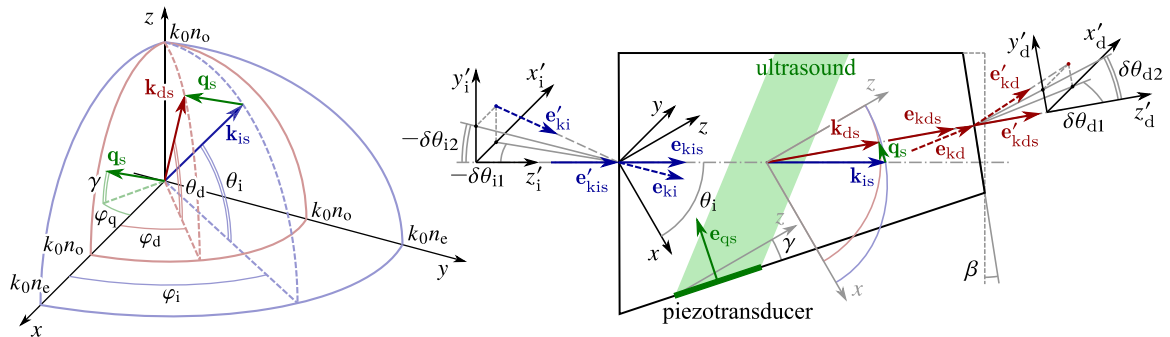


**Fig. 1.** General wavevector diagram (left part) and schematic configuration of the AO cell (right part) for anisotropic ( $e \rightarrow o$ ) AO interaction in uniaxial birefringent crystal.

$$\mathbf{e}_{\text{kdm}} = (\xi_a \mathbf{e}_{\text{ki}} + \eta_a \mathbf{e}_{\text{qs}}) / (1 + \chi), \quad (10)$$

$$|\Delta \mathbf{k}_m| = 2\pi n_o(\lambda_0) \chi / \lambda_0, \quad (11)$$

$$\chi = \sqrt{(\xi_a - \eta_a)^2 + 2\xi_a \eta_a (1 - A_a)} - 1, \quad (12)$$

where  $\xi_a$ ,  $\eta_a$ , and  $A_a$  are birefringent, spectral, and geometrical parameters:  $\xi_a = \xi(\lambda_0, \mathbf{e}_{\text{ki}})$ ,  $\eta_a = \lambda_0 f_s / [V(\mathbf{e}_{\text{qs}}) n_o(\lambda_0)]$ , and  $A_a = -\mathbf{e}_{\text{ki}} \cdot \mathbf{e}_{\text{qs}}$ .

The equation  $|\Delta \mathbf{k}_m(\lambda_0, \mathbf{e}_{\text{ki}})| = 0$  defines a locus of points in spectral-angular domain representing the wavelengths and directions of phase-matched components. We use the method similar to Refs. [13,14] to find the change of wavevector direction on its way through the AO cell including the refraction on the input and output facets. The input direction  $\mathbf{e}'_{\text{ki}}$  is defined by angles  $\delta\theta_{i1}$  and  $\delta\theta_{i2}$  (Fig. 1). We calculate values  $\mathbf{e}_{\text{kdm}}$ ,  $|\Delta \mathbf{k}_m|$ , and  $T$  as functions  $(\lambda_0, \delta\theta_{i1}, \delta\theta_{i2})$  using Eqs. (9)–(11). The results are shown in Fig. 2 for two geometries of AO anisotropic ( $e \rightarrow o$ ) interaction at  $\lambda_s = 600$  nm: collinear

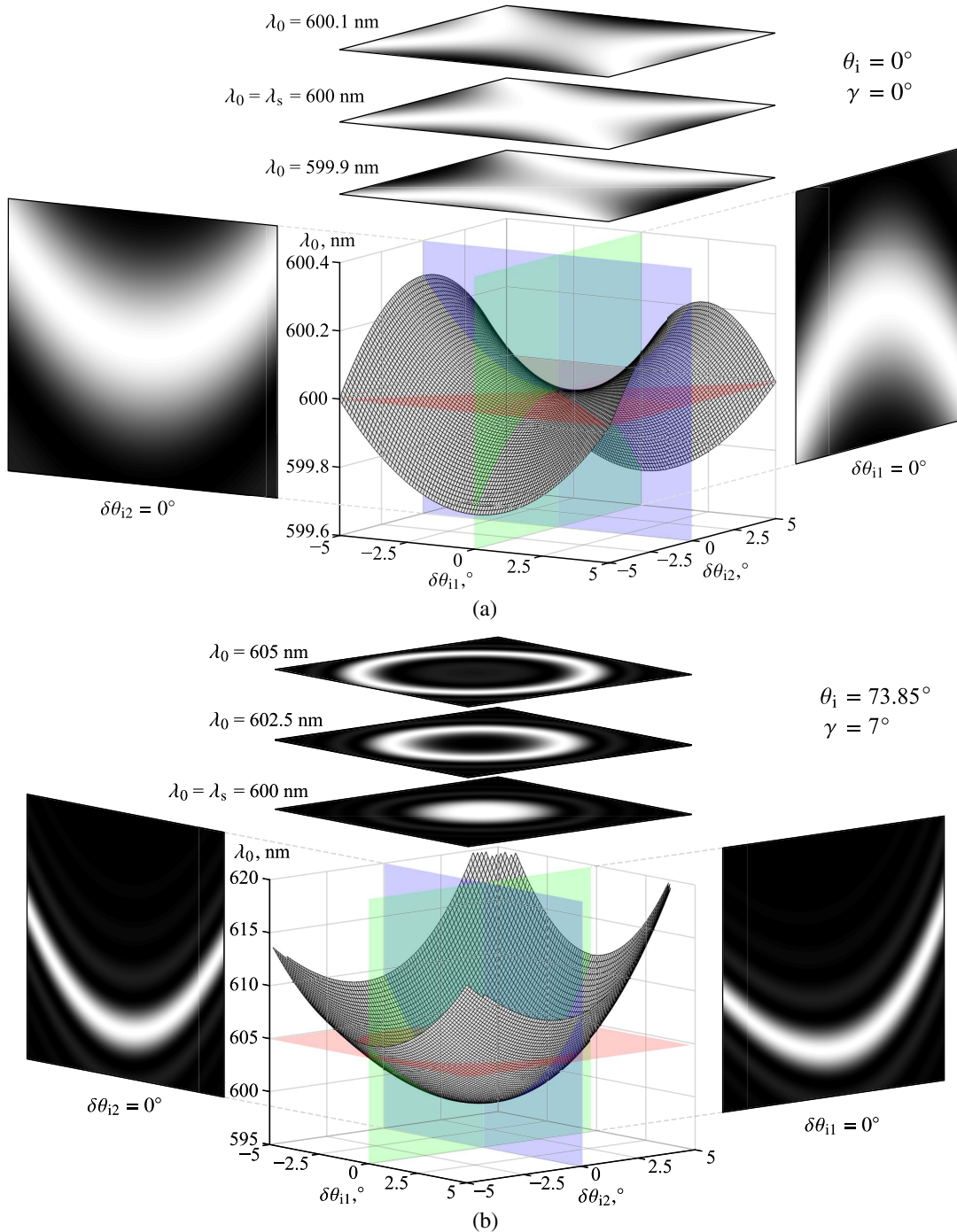


**Fig. 2.** Surface  $|\Delta \mathbf{k}_m(\lambda_0, \delta\theta_{i1}, \delta\theta_{i2})| = 0$  and the cross sections of the normalized transmission function  $T(\lambda_0, \delta\theta_{i1}, \delta\theta_{i2}) / (\Gamma L)^2$  for (a) collinear and (b) noncollinear geometries of AO anisotropic diffraction.

diffraction in calcium molybdate  $\text{CaMoO}_4$  [ $\varphi_i = \theta_i = \gamma = 0^\circ$ ,  $\varphi_q = 180^\circ$ ,  $\beta = 0^\circ$ ,  $L = 4$  cm, Fig. 2(a)] and wide-aperture noncollinear diffraction in paratellurite  $\text{TeO}_2$  [ $\varphi_i = 0^\circ$ ,  $\theta_i = 73.85^\circ$ ,  $\varphi_q = 180^\circ$ ,  $\gamma = 7^\circ$ ,  $\beta = 3.5^\circ$ ,  $L = 1$  cm, Fig. 2(b)]. For such tetragonal uniaxial crystals, axes  $x$ ,  $y$ , and  $z$  in Fig. 1 denote the  $[110]$ ,  $[-110]$ , and  $[001]$  axes, correspondingly.

The spectral dependence of the transmission function  $T(\lambda_0)$  for each direction  $(\delta\theta_{i1}, \delta\theta_{i2})$  follows the shape of the sinc-squared function as defined by Eq. (9), but the location of its maximum is defined by the shape of the surface  $|\Delta\mathbf{k}_m(\lambda_0, \delta\theta_{i1}, \delta\theta_{i2})| = 0$ . This spatio-spectral dependency is rather complicated and should be taken into account in imaging applications. The spectral and angular cross sections of the  $T$  function can be analyzed to calculate the spectral and angular bandwidth of the AO device [12,15,16], i.e., its spectral resolution and angular aperture, as well as to describe the angular structure of the output light beam at particular wavelength [9].

To illustrate the variety of the transmission function cross sections in the angular domain available in birefringent uniaxial crystal, we have calculated the map of images  $T(\delta\theta_{i1}, \delta\theta_{i2})$  depending on the wavevector directions of incident light  $\theta_i$  and ultrasound  $\gamma$  for  $e \rightarrow o$  diffraction in the  $x$ - $z$  plane ( $\varphi_i = 0^\circ$ ,  $\varphi_q = 180^\circ$ ) of  $\text{TeO}_2$  without regard to its effective photoelastic constants, i.e., in the case of 100% diffraction efficiency (Fig. 3). Two green rectangles mark the geometries shown in Fig. 2. The bottom right corner of the map is blank because there are no directions  $\mathbf{e}_{kds}$  satisfying phase-matching condition for the given  $\theta_i$  and  $\gamma$ . Since the wavevector direction of diffracted light is strictly defined by Eq. (10), all results can be similarly presented in  $(\lambda_0, \delta\theta_{d1}, \delta\theta_{d2})$  space. The number of bright pixels in the subimages in Fig. 3 varies due to the non-constant angular aperture. The wide-aperture geometries with the widest phase-matching bandwidth [7], which are in use for

imaging applications, are highlighted in Fig. 3 by a cyan arc. The presented map of phase-matching loci depicts all shapes allowed in uniaxial crystals (cross, ring, oval, stripe, arc, Y-shape, etc.) and corresponds to reference data [9,12]. These shapes result in a nonuniform light transmittance under AO interaction. The wider the angular aperture is, the more heterogeneous the image brightness becomes. Therefore, it makes sense to match the shapes of the image and transmission function. In a general case, the choice of AO interaction configuration depends on a combination of factors related to the application, including illumination spectrum, tuning range, requirements on angular aperture, spatial resolution, chromatic aberrations, etc. Similar maps may be obtained for other crystals, diffraction planes, and geometries of AO interaction.

### 3. EXPERIMENTAL STUDY

To demonstrate the specific spatio-spectral structure of the diffracted light beam, we have measured 2D angular transmission functions of the wide-aperture AO tunable filter (AOTF) based on the diffraction of light on a shear acoustic wave propagating at phase velocity  $V = 6.52 \times 10^4$  cm/s in  $\text{TeO}_2$  crystal with the following parameters: cut angle  $\gamma = 7^\circ$ , facet angle  $\beta = 2^\circ$ , acoustic walk-off angle is close to  $40^\circ$ , and linear aperture is 9 mm [17]. To tune the AOTF in the wavelength range 450–900 nm, ultrasound frequency from 130 to 65 MHz and average power 1 W have to be applied. The experimental setup is shown in Fig. 4. A monochromator MC (SF-46, LOMO) with a halogen light bulb and a diffusive plate D is used as a source of homogenous monochromatic light. To conjugate this light source with the AOTF, we used a  $4f$  system composed of the lenses L1 ( $f_1 = 18$  mm) and L2 ( $f_2 = 30$  mm). To ensure  $e \rightarrow o$  anisotropic AO interaction and to suppress undiffracted beams, two orthogonally oriented

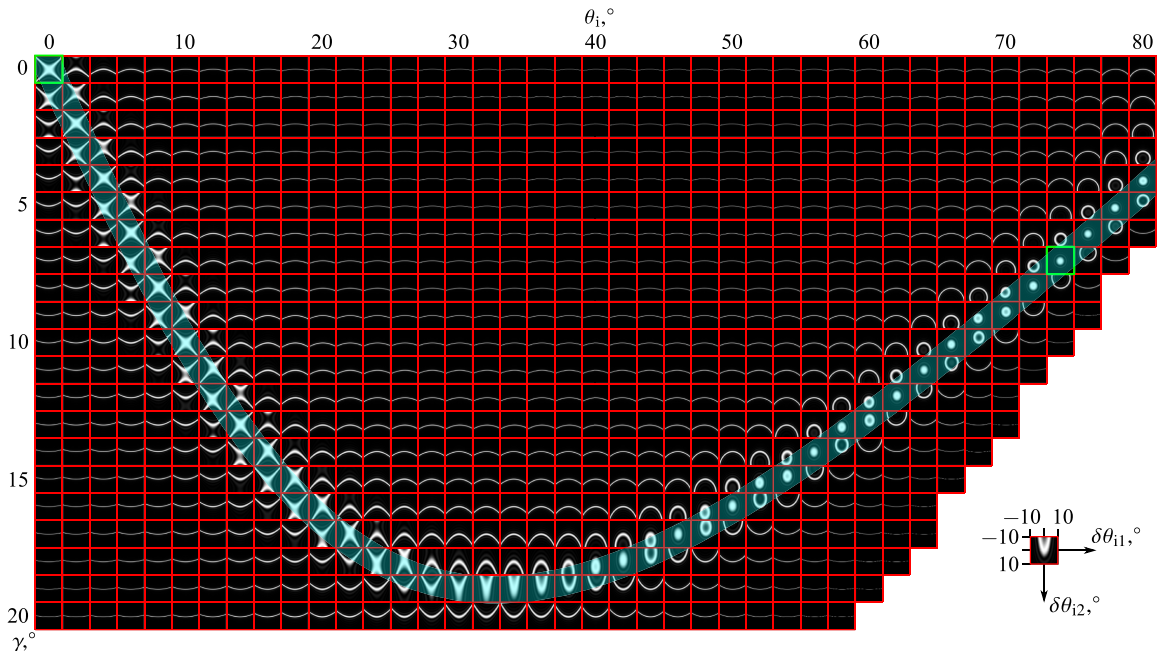


**Fig. 3.** Map of the normalized transmission functions  $T(\delta\theta_{i1}, \delta\theta_{i2})/(\Gamma L)^2$  in uniaxial crystal at  $\lambda_0 = \lambda_s = 600$  nm. The ranges of  $\delta\theta_{i1}$  and  $\delta\theta_{i2}$  in each subimage are  $\pm 10^\circ$ . Two green rectangles mark the geometries shown in Fig. 2. Wide-aperture geometries are highlighted by the cyan arc.



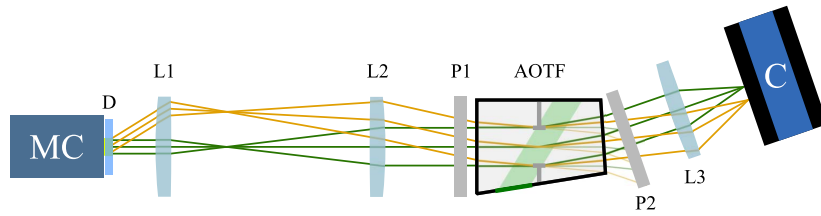


**Fig. 4.** Experimental setup for measuring 2D transmission functions: MC, monochromator; D, diffuser plate; L1, L2, L3, lenses; P1, P2, polarizers; AOTF, acousto-optical tunable filter; C, camera.

film polarizers P1 and P2 (XP42-200, Edmund Optics) have been installed. Lens L3 (TBL 25, The Imaging Source) focuses the diffracted beams onto the image sensor of color (DFK AFU420-CCS, The Imaging Source) or monochrome (DMK 37BUX178, The Imaging Source) camera C. To visualize the spatio-spectral structure of the diffracted beam, we have varied the central wavelength  $\lambda_{MC}$  of monochromator MC and acquired the transmitted light images while the ultrasonic frequency  $f_s$  applied to the AOTF had a fixed value.

The experimental images were transformed to angular coordinates  $(\delta\theta_{d1}, \delta\theta_{d2})$  with regard to focal length of lens L3 and

pixel pitch of the camera C, so that the intensity in the resulting image characterizes the AOTF transmission at the corresponding angles. To validate the described theoretical considerations against the experiment, we have modeled the diffracted light images under the same parameters. The simulated images  $I(\delta\theta_{d1}, \delta\theta_{d2}, \lambda_{MC})$  were obtained by summing the calculated transmission function values  $T(\lambda_0, \delta\theta_{d1}, \delta\theta_{d2})$  as follows:

$$I(\delta\theta_{d1}, \delta\theta_{d2}, \lambda_{MC}) = \int_{-\infty}^{+\infty} T(\lambda_0, \delta\theta_{d1}, \delta\theta_{d2}) L(\lambda_0, \lambda_{MC}) S(\lambda_0) d\lambda_0, \quad (13)$$

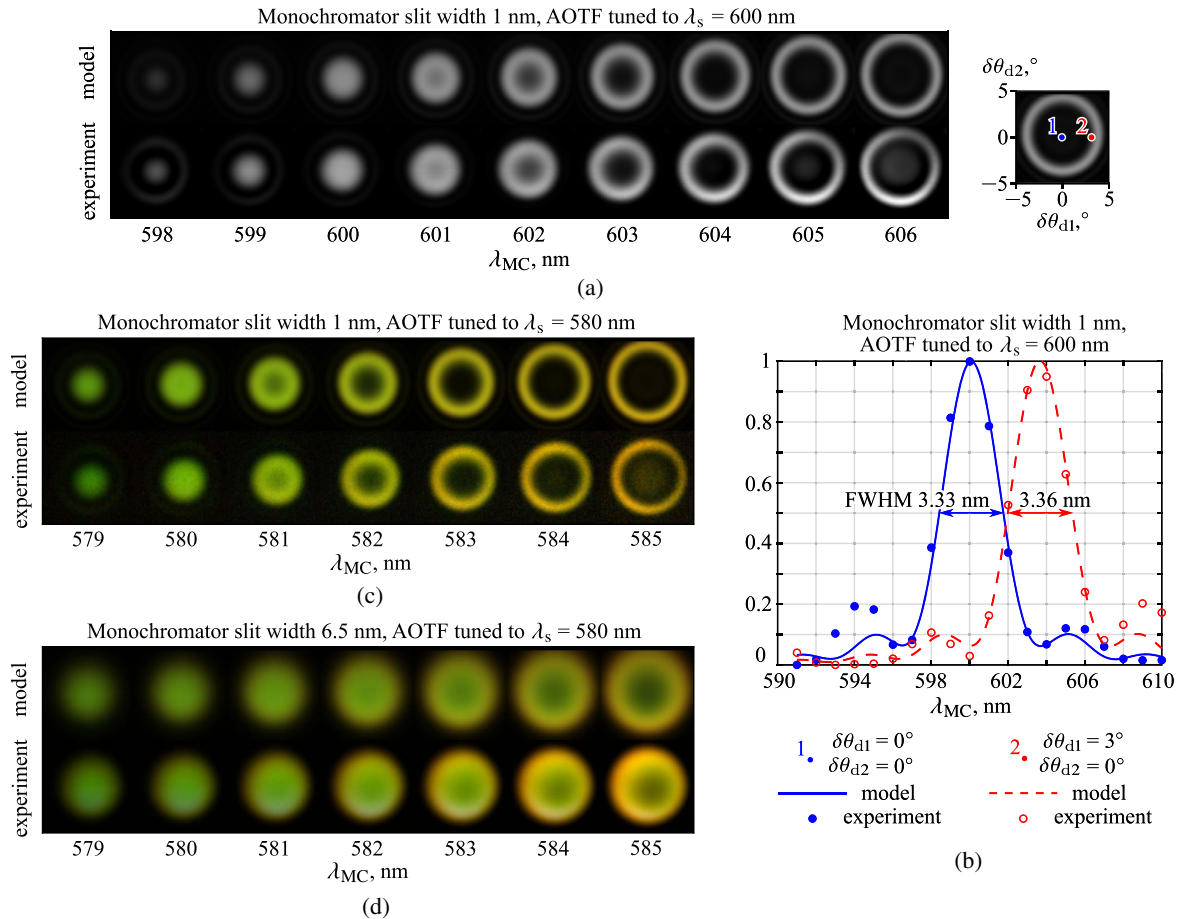


**Fig. 5.** (a) Simulated (upper row) and experimental (lower row) images  $I(\delta\theta_{d1}, \delta\theta_{d2})$  captured by the monochrome camera with the AOTF tuned to  $\lambda_s = 600$  nm ( $f_s = 85.5$  MHz) for different central wavelengths  $\lambda_{MC}$  of the monochromator MC with 1 nm slit width. The ranges of  $\delta\theta_{d1}$  and  $\delta\theta_{d2}$  in all subimages are  $\pm 5^\circ$ . (b) The dependence of normalized light intensity on  $\lambda_{MC}$  for points 1 and 2 shown in the right part of (a). The simulated and experimental images captured by the color camera with the AO cell tuned to  $\lambda_s = 580$  nm ( $f_s = 89.2$  MHz): for (c) 1 nm and (d) 6.5 nm slit width.

where  $L(\lambda_0, \lambda_{MC})$  is the spectral intensity of the incident light measured by spectrometer (Flame, Ocean Insight) when the central wavelength of the monochromator is set to  $\lambda_{MC}$ , and  $S(\lambda_0)$  is the normalized spectral sensitivity of the camera sensor.

The first experiment with a narrow monochromator slit (1 nm width) provides visualization of the spatio-spectral structure of the transmission function. The AOTF has been tuned to the fixed wavelength  $\lambda_s = 600$  nm ( $f_s = 85.5$  MHz) while the central wavelength of monochromator  $\lambda_{MC}$  was varied with 1 nm step [Fig. 5(a)]. Acquired experimental images [the lower row in Fig. 5(a)] correspond to the sections of the transmission function: from the circular spot when  $\lambda_{MC}$  is equal to  $\lambda_s = 600$  nm to expanding circles when  $\lambda_{MC}$  is 602, ..., 606 nm. When  $\lambda_{MC}$  is decreasing, the phase-matching condition Eq. (1b) cannot be satisfied, which results in the presence of the significant wave mismatch according to Eqs. (11) and (12). This appears as the fading of the central spot in the images caused by diffraction efficiency decrease. The simulated (upper row) and experimental (lower row) images were normalized to make their black levels and mean values coincident.

While the components with a wavelength  $\lambda_0$  equal to the center of the AOTF transmission window  $\lambda_s = 600$  nm pass through the center of the aperture, the mismatched components tend to pass differently. As can be seen from Fig. 5(b), the central wavelength of the transmission window for  $\delta\theta_{d1} = 3^\circ$  is shifted by about 3.5 nm. In practice, this means not only the spatio-spectral inhomogeneity but also a broader spectrum of a transmission function across the whole angular aperture. In our experiments, we have found out that even for a constant acoustic frequency applied to AOTF, the diffracted light spectrum may span almost within 9 nm, i.e., 2.5 times wider than the FWHM of AOTF transmission window  $T(\lambda_0)$  at the aperture center.

To emphasize the meaning of these AO interaction features for spectral analysis and to demonstrate the spectral properties of a filtered beam by visualizing the distribution of color hues, we have performed the same experiment with an RGB color camera. The experiment with a narrow slit (1 nm, 3 times less than the FWHM of the AOTF) allows visualization of isolated spectral components, with color variate from green to orange [Fig. 5(c)]. For broadened slit [6.5 nm, 2 times wider than the FWHM of the AOTF, Fig. 5(d)], the monochromatic transmission functions are superimposed and the acquired image looks different. While the intensity in the image seems to be homogeneous, it is actually spectrally nonuniform, which can be seen as the green hue of the circles fading to orange at the image periphery. Comparison of the upper and lower rows in Fig. 5 shows that the patterns match accurately. It means that the theoretical model and the simulation are adequate. We should note that for other AO interaction geometries and other configurations of the phase-matching locus [e.g., saddle-shaped surface as shown in Fig. 2(a)] the phase-matching condition can be also exactly satisfied for wavelengths shorter than  $\lambda_s$ , so the peripheral areas of the filtered image may shift toward the ultraviolet region as well as toward the infrared one.

#### 4. CONCLUSION

In this study, we have theoretically and experimentally studied the AO transmission function in uniaxial birefringent crystals,

shown the variety of its shapes, and demonstrated that its spectral and angular characteristics cannot be considered separately. This effect is inevitable and limits AO device performance, which is especially critical in imaging, beam shaping, and other applications related to significant angular aperture. For instance, in the collimating (telescopic) scheme [18], the spectral images obtained using AOTF demonstrate spectral inhomogeneity across the field of view and light transmission out of the selected band. Thus, to obtain monochromatic images in this scheme, one needs to decrease the angular aperture. In the confocal (telecentric) scheme [19], the described effect broadens the AOTF transmission window at all image points. This means that the numerical aperture should be decreased if narrowband filtration is necessary.

The analyzed dependence of the diffracted beam angular structure on the incident light wavelength for fixed sound frequency leads to the same patterns as its dependence on the ultrasound frequency for a fixed light wavelength, which was reported in Refs. [8,9].

The proposed approach to AOTF analysis is necessary for accurately estimating the key spectral-angular features of image transmission with respect to a complicated three-dimensional shape of phase-matching locus. The described technique allows choosing the optimal geometry of AO interaction and the shape of the crystal for a particular application with regards to required angular aperture, spectral resolution, image quality, and other factors. The obtained results are important for assessing the performance of AO devices in its design stage, so for the analysis of the light beam transformation in existing schemes containing AO cells.

**Funding.** Russian Science Foundation (19-19-00606).

**Disclosures.** The authors declare no conflicts of interest.

#### REFERENCES

1. V. I. Balakshy, V. N. Parygin, and L. E. Chirkov, *Physical Principles of Acousto-Optics* (Radio i Svyaz, 1985).
2. K. W. Gamalath and G. Jayawardena, "Diffraction of light by acoustic waves in liquids," *Int. Lett. Chem. Phys. Astron.* **4**, 39–57 (2012).
3. W. Dürr, "Acousto-optic interaction in gases and liquid bases in the far infrared," *Int. J. Infrared Millim. Waves* **7**, 1537–1558 (1986).
4. J. Xu and R. Stroud, *Acousto-Optic Devices: Principles, Design, and Applications* (Wiley, 1992).
5. A. P. Goutzoulis and D. R. Pape, eds., *Design and Fabrication of Acousto-Optic Devices* (Marcel Dekker, 1994).
6. V. I. Balakshy, "Application of acousto-optic interaction for holographic conversion of light fields," *Opt. Laser Technol.* **28**, 109–117 (1996).
7. I. Chang, "Acousto-optic devices and applications," *IEEE Trans. Ultrason.* **23**, 2–21 (1976).
8. M. D. McNeill and T.-C. Poon, "Gaussian-beam profile shaping by acousto-optic Bragg diffraction," *Appl. Opt.* **33**, 4508–4515 (1994).
9. V. I. Balakshy and D. E. Kostyuk, "Acousto-optic image processing," *Appl. Opt.* **48**, C24–C32 (2009).
10. V. B. Voloshinov, "Anisotropic light diffraction on ultrasound in a tellurium dioxide single crystal," *Ultrasonics* **31**, 333–338 (1993).
11. A. Yariv and P. Yeh, *Optical Waves in Crystals* (Wiley, 1984), Vol. 5.
12. V. Pozhar and A. Machihin, "Image aberrations caused by light diffraction via ultrasonic waves in uniaxial crystals," *Appl. Opt.* **51**, 4513–4519 (2012).
13. H. Zhao, C. Li, and Y. Zhang, "Three-surface model for the ray tracing of an imaging acousto-optic tunable filter," *Appl. Opt.* **53**, 7684–7690 (2014).

14. M. N. Kozun, A. E. Bourassa, D. A. Degenstein, and P. R. Loewen, "A multi-spectral polarimetric imager for atmospheric profiling of aerosol and thin cloud: prototype design and sub-orbital performance," *Rev. Sci. Instrum.* **91**, 103106 (2020).
15. D. R. Suhre, M. S. Gottlieb, L. H. Taylor, and N. T. Melamed, "Spatial resolution of imaging noncollinear acousto-optic tunable filters," *Opt. Eng.* **31**, 2118–2122 (1992).
16. V. B. Voloshinov, "Imaging experiments based on application of non-collinear tunable acousto-optic filters," *Proc. SPIE* **3584**, 116–127 (1999).
17. V. I. Batshev, A. S. Machikhin, A. B. Kozlov, S. V. Boritko, M. O. Sharikova, A. V. Karandin, V. E. Pozhar, and V. A. Lomonov, "Tunable acousto-optic filter for the 450–900 and 900–1700 nm spectral range," *J. Commun. Technol. Electron.* **65**, 800–805 (2020).
18. A. Machikhin, V. Batshev, and V. Pozhar, "Aberration analysis of AOTF-based spectral imaging systems," *J. Opt. Soc. Am. A* **34**, 1109–1113 (2017).
19. D. R. Suhre, L. J. Denes, and N. Gupta, "Telecentric confocal optics for aberration correction of acousto-optic tunable filters," *Appl. Opt.* **43**, 1255–1260 (2004).